Available online at www.sciencedirect.com

SciVerse ScienceDirect

Ceramics International 39 (2013) 7415–7424

CERAMICS INTERNATIONAL

www.elsevier.com/locate/ceramint

Effect of lanthanide doping on crystal phase and near-infrared to near-infrared upconversion emission of Tm^{3+} doped $KF–YbF_3$ nanocrystals

Y.C. Li, L.W. Yang*, S.X. Yu, Y. Li, P. Yang, X.L. Wei, J.X. Zhong

Hunan Key Laboratory of Micro-Nano Energy Materials and Devices, and Faculty of Materials and Optoelectronic Physics, Xiangtan University, Hunan 411105, China

Received 9 January 2013; received in revised form 22 February 2013; accepted 25 February 2013
Available online 7 March 2013

Abstract

Tm^{3+} doped $KF–YbF_3$ nanocrystals were synthesized by a hydrothermal method using oleic acid as a stabilizing agent at 190 °C. The influence of Gd^{3+} and Sm^{3+} content on the phase structure and upconversion (UC) emission of the final products was investigated by X-ray diffraction (XRD), transmission electron microscopy (TEM) and UC spectra. XRD analyses and TEM observations evidence that the phase and size of the as prepared Tm^{3+} doped $KF–YbF_3$ nanocrystals are closely related to the Gd^{3+} doping content. Without Gd^{3+} impurity, the undoped nanocrystals crystallize in orthorhombic KYb_2F_7 with an average diameter of 42 nm. When the Gd^{3+} doping is below 10 mol%, the orthorhombic KYb_2F_7 nanocrystals grow up. However, with Gd^{3+} addition beyond about 30 mol%, the complete phase transformation from orthorhombic KYb_2F_7 to cubic $KGdF_4$ occurs in the final products. Under the excitation of a 980 nm laser diode, the as prepared Tm^{3+} doped nanocrystals exhibit strong near-infrared UC emission at 800 nm. Particularly, the intensity of high energy UV and blue UC emissions of Tm^{3+} ions in Tm^{3+} doped KYb_2F_7 nanocrystals are selectively reduced compared to the NIR emission at 800 nm by co-doping a small amount of Sm^{3+} ions into the host matrix. Possible dynamic processes for UC emissions in Tm^{3+} doped nanocrystals are discussed in detail.

Keywords: Hydrothermal method; Upconversion; Phase transformation; Lanthanide doping

1. Introduction

Lanthanide (Ln^{3+}) ions doped up-conversion (UC) nanocrystals attract more and more attention because of their potential applications in multi-color displays [1,2], optical processing sensors [3], solar cells [4,5], and especially, luminescencent labels for bioimaging and biomedicine [6–8]. At present, many host materials, such as oxides, phosphates, vanadates, fluorides, and chlorides, have an ability to demonstrate highly efficient multicolor UC emissions under the excitation of a near-infrared (NIR) laser diode (LD) with wavelength of 980 nm [9,10]. Among them, fluorides have been extensively investigated due to strong UC emissions. By precisely controlling the doping type and concentration of Ln^{3+} ions, multicolor UC emissions spanning infrared to deep ultraviolet including white light have been observed from fluoride nanocrystals [8,9,11–19]. Very interestingly, in these systems, Ln^{3+} doping also has great effect on the crystal phase and size along with the UC emission [2,20–22]. For instance, Wang et al. [2] demonstrated that the size reduction down to ten nanometers, phase transformation from cubic to hexagonal of $NaYF_4$ nanocrystals could be rationally tuned by introducing trivalent Gd^{3+} ions at precisely defined concentrations. However, studies on the influence of Ln^{3+} doping in fluoride nanocrystals have mostly been restricted to $NaLnF_4$ system and there have been few investigations on other important fluorides such as LnF_3, $MF–LnF_3$ (M = Li, K, and Cs), and $AF_2–LnF_3$ (A being a group-II element).

Ln^{3+}-doped UC nanocrystals have demonstrated a great potential as optical contrast agents for bio-imaging due to the

*Corresponding author. Tel.: +86 731 58292195.
E-mail addresses: ylwxtu@xtu.edu.cn, ylwnju@163.com (L.W. Yang).

0272-8842/$ - see front matter © 2013 Elsevier Ltd and Techna Group S.r.l. All rights reserved.
http://dx.doi.org/10.1016/j.ceramint.2013.02.085

fact that the excitation light (~980 nm) falls well within the biological transmission window leading to increased penetration depths and reduced autofluorescence. In addition, Ln^{3+}-doped UC nanocrystals have superior photo and chemical stability and ability to display multicolored, spectrally distinguished UC emission under excitation with low-cost NIR LD. Up to now, several groups have reported the applications to biology including both in vitro and in vivo imaging [8]. Unfortunately, the output emissions in the range of the visible region increase the background scattering leading to reduced resolution in the imaging process. Very recently, Yb^{3+}–Tm^{3+} co-doped fluoride nanocrystals with strong NIR-to-NIR UC emission are of great interest because in these UC nanocrystals the UC emission peaked at 800 nm and the excitation at 980 nm are both within the spectral range of 750–1000 nm, which is considered the "window of optical transparency" for biological tissues [23–26]. Hence, these Yb^{3+}–Tm^{3+} co-doped nanocrystals with strong NIR-to-NIR UC emission allows us to perform high-contrast in vitro and in vivo optical bioimaging with a relatively high tissue penetration depth [26]. Nevertheless, in addition to the strong NIR emission, the Tm^{3+} ions in the fluoride nanocrystals emit relatively strong emissions in the blue region (~475 and 450 nm) and weak emissions in the red region (~650 nm) and ultraviolet region (360 nm), which inevitably affect the resolution of the imaging process. Hence it is highly desirable to develop an approach to improve NIR (~800 nm) to visible/UV emission ratios so as to further enhance the resolution of the bio-imaging process [24].

The KF–LnF_3 system is interesting due to both its structural and optical properties. Despite recent research on the KF–LnF_3 nanocrystals [12], the effect of Ln^{3+} doping on crystal phase and NIR to NIR UC emission in these nanocrystals has been rarely reported. In this work, Tm^{3+} doped KF–YbF_3 nanocrystals are synthesized by a hydrothermal method using oleic acid as a stabilizing agent at 190 °C. The influence of Gd^{3+} and Sm^{3+} content on the phase structure and NIR UC emission of Tm^{3+} doped KF–YbF_3 nanocrystals is investigated in detail.

2. Experimental

The synthesis was carried out using commercially available reagents. The $Ln(NO_3)_3.6H_2O$ with the grade of 99.99% were supplied by Sinopharm Chemical Reagent Company. All other chemicals were analytical grade and were used as received without further purification. In a typical synthesis, 2 ml of an aqueous solution containing 17.5 mmol KOH, 12 ml alcohol and 15 ml oleic acid were added to a beaker sequentially under vigorous stirring to form a transparent homogeneous solution at room temperature. Then, 2.24 ml of 0.5 M $Ln(NO_3)_3$ (1.12 mmol) with pre-designed Yb^{3+} and Gd^{3+} or Sm^{3+} content were poured into the translucent solution under vigorous stirring and the obtained mixture was aged for 10 min at room temperature. At last, 5 ml of 1.2 M KF (6 mmol) were added under vigorous stirring until a translucent solution was obtained. After agitating for another 30 min, the colloidal solution was transferred to a 50 ml stainless Teflon-lined autoclave. The reactions were conducted in an oven at 210 °C for 20 h. After the reaction, the products deposited on the bottom of the Teflon vessel were collected and washed with ethanol and deionized water several times to remove other remnants, and then dried at 70 °C for 24 h.

The crystal structures of the synthesized samples were determined by X-ray diffraction (XRD, D/Max 8550) using a copper K_α radiation source ($\lambda = 0.154$ nm) at 40 kV and 40 mA. The morphologies and microstructures were characterized by transmission electron microscopy (TEM, JEOL 2100) equipped with selected area electron diffraction (SAED) and an Oxford energy dispersive X-ray spectroscopy (EDS) system at an acceleration voltage of 200 KV. The TEM specimens were prepared by directly drying a drop of a dilute cyclohexane dispersion solution of the as-prepared products on the surface of a carbon-coated copper grid. The UC spectra were recorded on a spectrophotometer (R-500) under excitation by a 980 nm laser diode (LD) after the powder samples were compressed into smooth slices. The fluorescence spot of the parallel laser beam on the sample had a diameter of about 0.4 cm and the measurements were performed at room temperature. The UC photographic images of the samples were taken by a digital camera (Canon PowerShot A720, Japan) without adding any filter.

3. Results and discussion

Usually, for K, Yb and F ternary system, the crystal phase of the final products strongly depends on the experimental condition. There are several reported crystal phases including monoclinic, orthorhombic and cubic. The XRD patterns of as prepared KF–LnF_3 nanocrystals with different Gd^{3+} doping concentrations are shown in Fig. 1. Compare to the standard PDF card data, the XRD peaks from the sample without Gd^{3+} doping match well up to standard orthorhombic KYb_2F_7 (JCPDS 27-0459). The results indicate that under our experimental condition, for pure K, Yb and F ternary system, the thermodynamically stable phase is orthorhombic KYb_2F_7. From the XRD results, one can find that when the concentration of Gd^{3+} doping is less than 10 mol%, Gd^{3+} doping has no obvious influence on the orthorhombic phase of the final products. However, the diffraction peaks ascribed to the orthorhombic KYb_2F_7 become sharper with the addition of Gd^{3+} impurity, manifesting the increase of the average crystallite size. Especially, one weak and broad diffraction peak at 28° appears, implying the existence of nanocrystals with smaller size in the products. With increasing Gd^{3+} doping concentration up to 30 mol%, one can see that the XRD peaks ascribed to the orthorhombic KYb_2F_7 disappear notably. When the concentration of Gd^{3+} doping is more than 30 mol%, the XRD peaks from the sample

match well up to cubic $KGdF_4$ and no obvious XRD peaks from the orthorhombic KYb_2F_7 can be observed. With further increasing Gd^{3+} doping concentration, all samples crystallize in the cubic phase and no other impurity phase occurs. The results reveal that the complete phase transformation from orthorhombic KYb_2F_7 to cubic $KGdF_4$ occurs in the final products due to the Gd^{3+} doping.

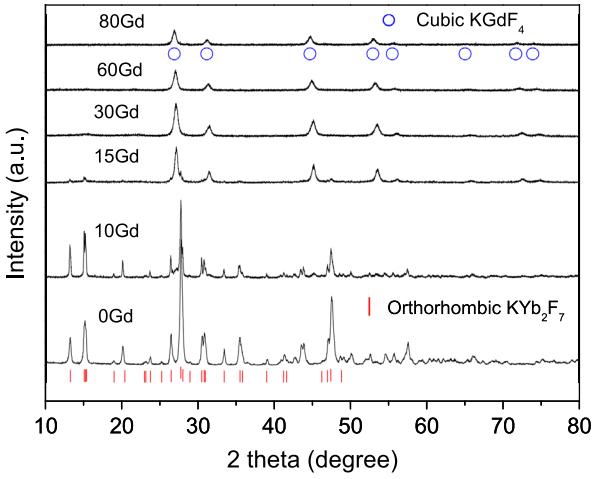

Fig. 1. Typical XRD patterns of Tm^{3+} doped KF–YbF_3 nanocrystals with different Gd^{3+} concentrations. The data of cubic $KGdF_4$ and orthorhombic KYb_2F_7 are resourced from Ref. [12] and standard XRD card (JCPDS no. 27-0459), respectively.

The morphologies and microstructures of the samples with different Gd^{3+} doping concentrations are further examined by TEM observations. Fig. 2(a) depicts typical TEM image of the synthesized orthorhombic KYb_2F_7 sample without Gd^{3+} doing, displaying non-uniform rod-shape morphology with small aspect ratio. The average size of the nanocrystals is determined to be 42 nm from the statistical histogram as shown in Fig. 2(c). Fig. 2(b) displays typical high resolution TEM image of the nanocrystals. The lattice arrangement in the nanocrystals is clearly visible suggesting a highly crystalline nature. The distance between the fringes (d-spacing) is 3.39 Å, which corresponds to the distance of the (320) plane of the standard orthorhombic KYb_2F_7. Fig. 2(d) is the corresponding EDS results of the synthesized orthorhombic KYb_2F_7 sample. One can find that the major constituents are K, Yb, and F (see Fig. 2d), which are consistent with their real elemental components. Fig. 3(a) depicts typical TEM image of the synthesized cubic Gd^{3+} (80%mol)

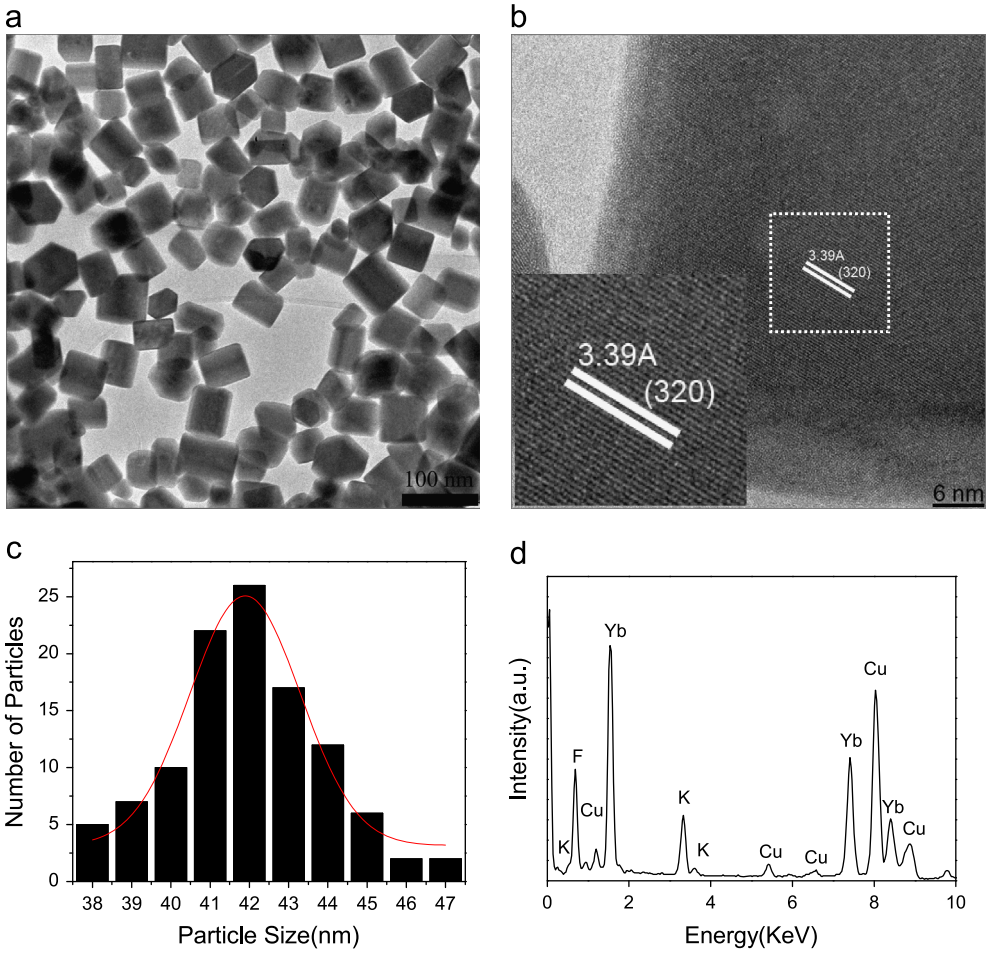

Fig. 2. (a) Typical TEM image and (b) high resolution TEM image acquired from the orthorhombic KYb_2F_7 nanocrystals. Inset shows the enlarged image of the marked regions. (c) Statistical histogram of the nanocrystal size distribution. (d) EDS spectrum of the orthorhombic KYb_2F_7 nanocrystals. Note that the signals for Cu come from the copper TEM grid.

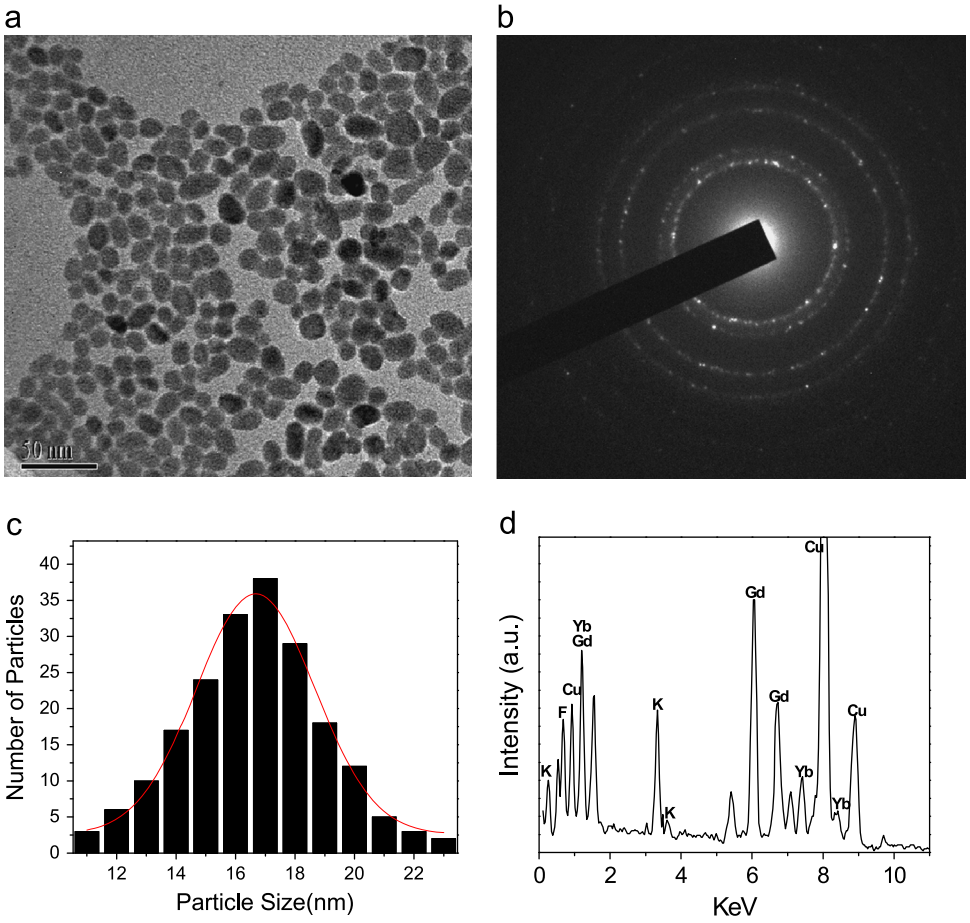

Fig. 3. (a) TEM image and (b) SEAD pattern acquired from as-synthesized cubic Gd^{3+} (80%mol) doped $KYbF_4$ nanocrystals. (c) Statistical histogram of the nanocrystal size distribution. (d) EDS spectrum of the Gd^{3+} doped $KYbF_4$ nanocrystals. Note that the signals for Cu come from the copper TEM grid.

doped $KYbF_4$ nanocrystals, revealing that the nanocrystals are nearly spherical in shape. The average size of the nanocrystals is determined to be 17 nm from the statistical histogram (see the Fig. 3c), which also shows the narrow size distribution and that the size of the majority of the nanocrystals is 12–22 nm. Fig. 3(b) is typical SEAD patterns of the cubic Gd^{3+} (80%mol) doped $KYbF_4$ nanocrystals. The observed distinct SEAD rings can be well indexed according to the standard cubic $KGdF_4$, which imply that the as-prepared nanocrystals crystallize in cubic phase with high-quality. Fig. 3(d) shows the EDS spectra, which confirms that the major constituents of the cubic Gd^{3+} (80%mol) doped $KYbF_4$ nanocrystals are K, Gd, F, and Yb. Fig. 4(a) and (c) show typical low-magnified TEM images of the synthesized sample doped with 10 mol% Gd^{3+}. Rod-shaped nanocrystals with large size beyond 100 nm and small particles can be observed, implying the existence of two phases, which is consistent with the XRD results. The SEAD patterns shown in Fig. 4(b) reveals that the rod-shapes nanocrystals with large size crystallize in orthorhombic phase KYb_2F_7 with high-quality. However, interestingly, the SEAD rings obtained from the small particles (see the Fig. 4d) are similar with that from cubic Gd^{3+} (80%mol) doped $KYbF_4$ nanocrystals. Further EDS spectra (see Fig. 4e) confirm that the major constituents of the small particles include K, Yb, Gd and F. Therefore, the small particles are Gd^{3+} doped cubic $KYbF_4$. The results imply that under the same experimental condition, cubic $KGdF_4$ is more thermodynamically stable than orthorhombic KYb_2F_7. As a result, the phase transformation from orthorhombic phase to cubic one in the final products occurs readily for K, Yb and F ternary system via Gd^{3+} doping.

Fig. 5 shows UC luminescence spectra of Tm^{3+} (0.5 mol%) doped KF–LnF_3 nanocrystals with different Gd^{3+} doping concentrations under excitation by a 980 nm LD. Four emission bands in the range from 350 nm to 850 nm can be observed. The blue emissions centered at 451 and 475 nm correspond to $^1D_2 \rightarrow {}^3F_4$ and $^1G_4 \rightarrow {}^3H_6$ transitions of Tm^{3+} ions, respectively. The weak red emissions centered at 650 nm and 695 nm are assigned to $^3F_2 \rightarrow {}^3H_6$ and $^3F_3 \rightarrow {}^3H_6$ transitions of Tm^{3+} ions, respectively. The weak ultraviolet emission at 362 nm originates from the $^1D_2 \rightarrow {}^3H_6$ transition of Tm^{3+} ions. Besides these weak ultraviolet, blue and red emissions, a strong NIR UC emission at 800 nm corresponding to $^3H_4 \rightarrow {}^3H_6$ transition of Tm^{3+} ions are also observed in all samples. These transitions occur via energy transfer (ET) from Yb^{3+} ions,

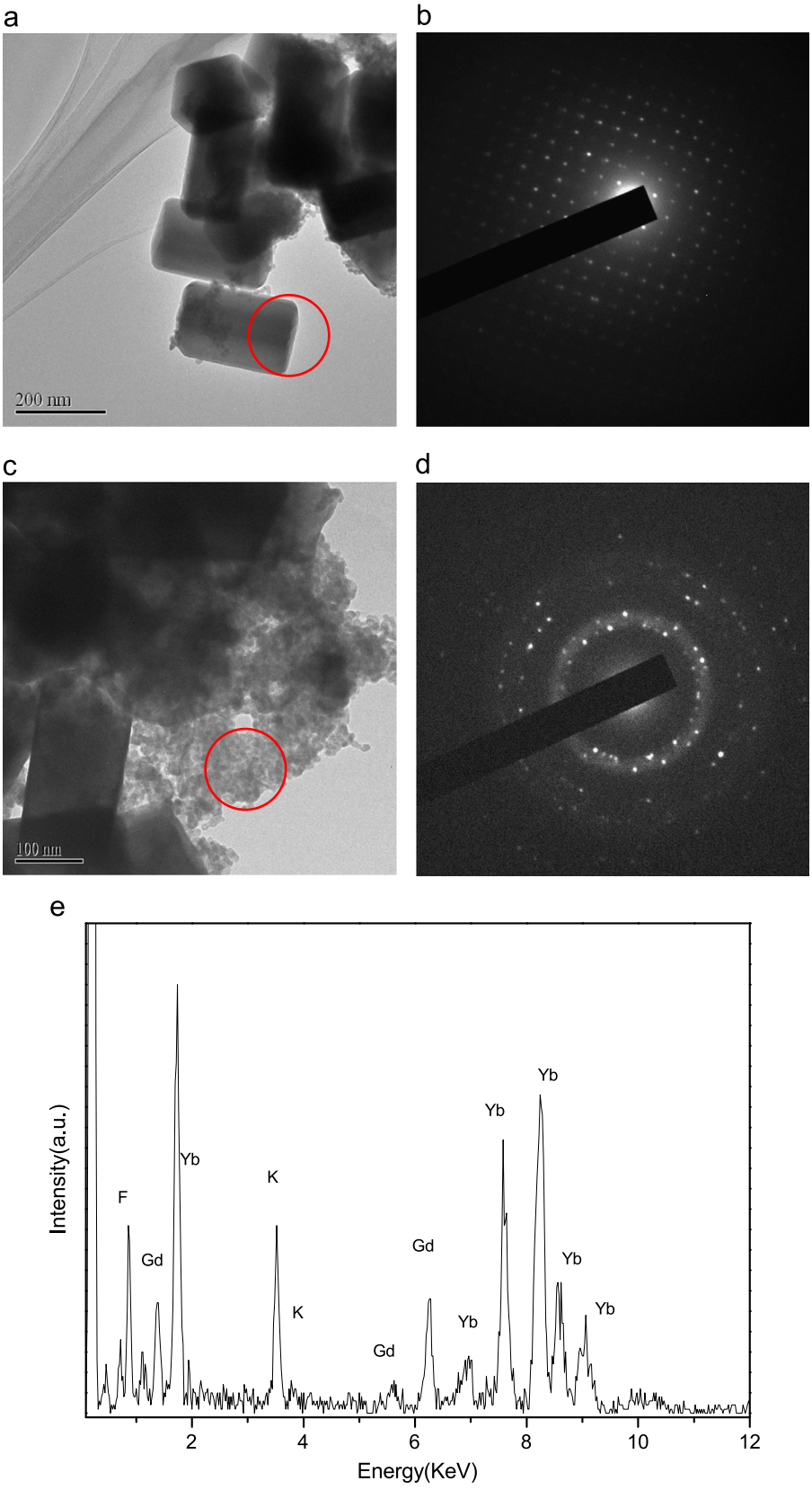

Fig. 4. (a) and (c) Typical TEM images acquired from the as-synthesized Tm^{3+} doped KF–YbF_3 nanocrystals doping with 10 mol% Gd^{3+}. (b) and (d) The corresponding SEAD patterns of the marked area in (a) and (c), respectively. (e) EDS spectrum of the marked area in (b).

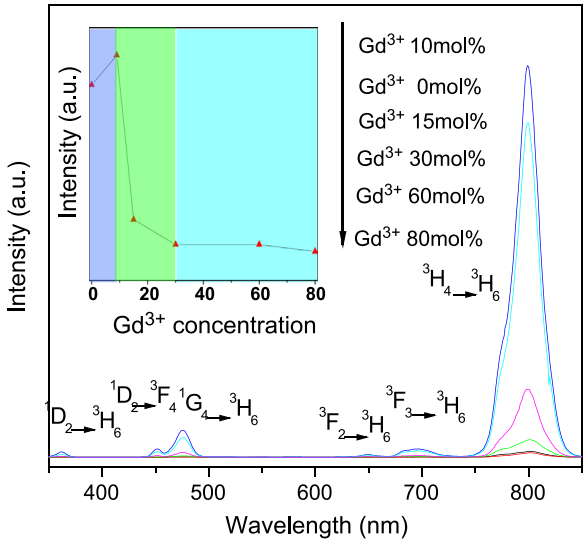

Fig. 5. UC emission spectra of Tm^{3+} (0.5 mol%) doped KF–YbF_3 nanocrystals with different Gd^{3+} concentrations under the excitation of a 980 nm LD. The inset shows the dependence of NIR UC emission at 800 nm of Tm^{3+} (0.5 mol %) doped KF–YbF_3 nanocrystals on the Gd^{3+} doping concentration.

which are used as sensitizers for Tm^{3+} ions as the Yb^{3+} ions possess higher absorption coefficient at 980 nm. In addition, from the spectra and the dependence of NIR UC emission at 800 nm on the Gd^{3+} doping concentrations in Tm^{3+} (0.5 mol%) doped KF-LnF_3 nanocrystals (see the inset of Fig. 5), one can find that the luminescence intensities of the samples firstly increase with increasing Gd^{3+} doping concentration to 10 mol%, then decrease notably with increasing Gd^{3+} doping concentration to 15 mol%, finally exhibits a mild decrease with further increasing Gd^{3+} doping content. Usually, the UC luminescence intensities in Yb^{3+}–Tm^{3+} doped nanocrystals depend strongly on crystal structure and size of host materials besides Yb^{3+} ions concentration. Herein the influence of Yb^{3+} ions concentration should be minor since all samples have high Yb^{3+} ions concentration beyond 20%mol, which makes the ET from Yb^{3+} ions to Tm^{3+} efficient. Therefore, the initial increase in emission intensity can be associated with the increase of size in the obtained orthorhombic KYb_2F_7 nanocrystals according to the aforementioned XRD and TEM results. For the subsequent notable decrease in emission intensity, both the reduction in crystal size and the transition of crystal structure in the final products play important role since its primary component for the sample with Gd^{3+} doping concentration of 15 mol% is cubic Gd^{3+} doped $KYbF_4$ nanocrystals with smaller crystal size from the XRD results. The final mild decrease in emission intensity is primarily attributed to the reduction of crystal size in the obtained cubic nanocrystal. Smaller nanocrystals tend to have increased surface quenching sites and thus suppress UC luminescence by enhanced nonradiative ET processes of the luminescent Ln^{3+} ions [14,27–30].

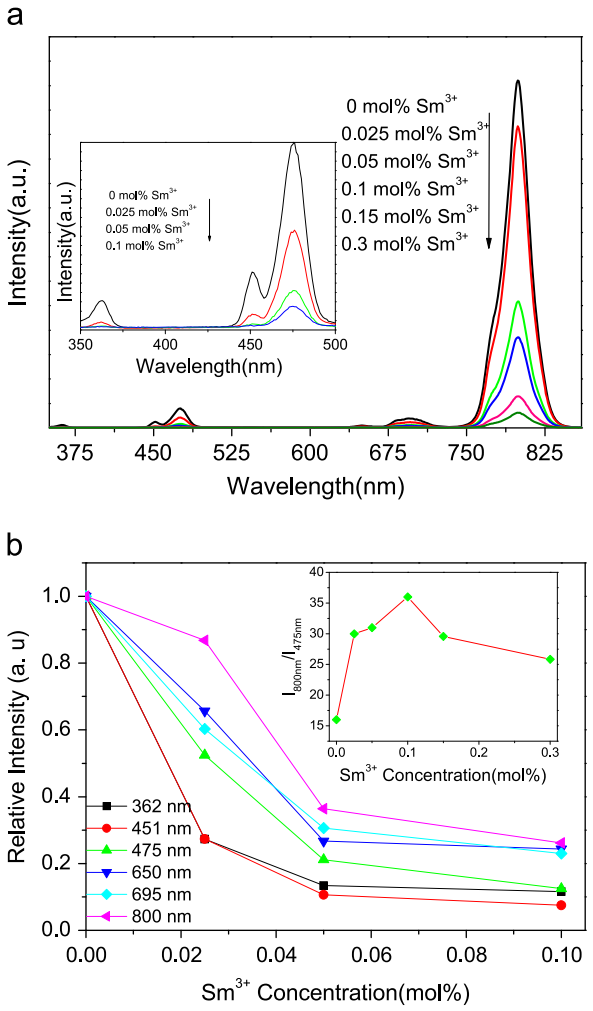

Fig. 6. (a) UC emission spectra of Tm^{3+} doped KYb_2F_7 nanocrystals with different Sm^{3+} doping concentrations. Inset shows the enlarged UV and blue regions of the emission spectra. (b) Plot of relative UC emission intensity versus the Sm^{3+} ion concentrations. Inset shows the relative intensity ratio between NIR emission at 800 nm and blue UC emission at 475 nm.

According to first-principle calculation, Wang et al. [2] proposed that the influence of Ln^{3+} doping on the crystal phase and size of the final nanocrystals arose from a strong dependence on the size and dipole polarizability of the substitutional dopant ion. Besides Gd^{3+} ion, several other Ln^{3+} ions including Nd^{3+} and Sm^{3+} have similar ability to tune crystal phase and size of the final products. However, due to the quenching of excitation energy through efficient ET from Yb^{3+} to ^6F_J manifolds of Sm^{3+} or ^4I_J manifolds of Nd^{3+}, the intensity of UC luminescence is completely depressed in Tm^{3+} doped KF–LnF_3 nanocrystals co-doping with Sm^{3+} or Nd^{3+} beyond 10 mol%. Fortunately, in our experiments, by co-doping only a small amount of Sm^{3+} ions into the host matrix, the UC emissions of KF–LnF_3 nanocrystals exhibit very interesting features. Fig. 6(a) shows UC luminescence spectra of as-prepared Tm^{3+} (1 mol%): KYb_2F_7 nanocrystals with different Sm^{3+} doping concentrations under

excitation by a 980 nm LD. One can find that upon additionally doping small concentrations of Sm^{3+} ions (0.025% or 0.05%) into the Tm^{3+} doped KYb_2F_7 nanocrystals, the UC emission intensities of the UV (362 nm) and blue emissions (451 nm) are drastically reduced compared to the emissions at 475 nm, 650 nm, 695 nm and 800 nm. To obtain quantitative information on the effect of Sm^{3+} ions on the UC emissions from Tm^{3+}/Sm^{3+} co-doped KYb_2F_7 nanocrystals, we have calculated the relative decrease in the emission intensities of the peaks with respect to the Tm^{3+} doped KYb_2F_7 nanocrystals (without Sm^{3+} ions). The graph displayed in Fig. 6(b) clearly indicates that the doping of Sm^{3+} ions lead to a larger reduction of the high energy UV (362 nm) and blue (450 nm) emissions compared with that of the NIR emission at 800 nm. The emissions centered at 650 nm, 695 and 475 nm show a moderate decrease in the intensity. Especially, NIR (~800 nm) to visible (475 nm) emission ratios is enhanced notably compared with that of the Tm^{3+} doped KYb_2F_7 nanocrystals (without Sm^{3+} ions) when Sm^{3+} doping concentrations is below 0.1 mol% (see the inset of Fig. 6b). However, with further increasing Sm^{3+} doping concentrations, NIR (~800 nm) to visible (475 nm) emission ratios decrease. In addition, no characteristic Sm^{3+} signature is observed from the UC emission spectra. The two abnormal features imply that there exists quenching mechanisms between Sm^{3+} and Tm^{3+}.

Usually, for the UC emissions of Tm^{3+} sensitized by Yb^{3+}, the following multiple phonon-assisted ET processes from Yb^{3+} ions to Tm^{3+} ions [see Fig. 7(a)] are responsible for the population of upper excited $^3H_4$, $^3F_2/^3F_3$, $^1G_4$ and $^1D_2$ states of Tm^{3+} ions [13,31,32].

$$^2F_{5/2}(Yb^{3+})+{}^3H_6(Tm^{3+})\rightarrow{}^3H_5(Tm^{3+})+{}^2F_{7/2}(Yb^{3+})+\text{-phonon energy } (3100\ cm^{-1})\sim{}^3F_4(Tm^{3+})+\text{multiphonon relaxation (about 2 phonons)} \quad (1)$$

$$^2F_{5/2}(Yb^{3+})+{}^3F_4(Tm^{3+})\rightarrow{}^3F_2/^3F_3\ (Tm^{3+})+{}^2F_{7/2}(Yb^{3+})+\text{phonon energy } (0\ cm^{-1})\sim{}^3H_4(Tm^{3+})+\text{multiphonon relaxation (about 6 phonons)} \quad (2)$$

$$^2F_{5/2}(Yb^{3+})+{}^3H_4(Tm^{3+})\rightarrow{}^1G_4(Tm^{3+})+{}^2F_{7/2}(Yb^{3+})+\text{phonon energy } (1300\ cm^{-1}) \quad (3)$$

$$^2F_{5/2}(Yb^{3+})+{}^1G_4(Tm^{3+})\rightarrow{}^1D_2(Tm^{3+})+{}^2F_{7/2}(Yb^{3+})+\text{-phonon energy}(3000^{-1}) \quad (4)$$

Subsequently, when the $^3H_4$, $^3F_2/^3F_3$, $^1G_4$ and $^1D_2$ excited states are radiatively decayed to the ground state or the lowest excited state of $^3F_4$, NIR, red, blue and ultraviolet UC emissions are generated. According to the aforementioned spectral results, it is clear that selective suppression of the intensity of the higher energy emissions over the NIR emission is realized via doping small concentrations of Sm^{3+} ions. These observations suggest a faster depopulation of the $^1D_2$ and $^1G_4$ states via some additional nonradiative channels due to the addition of Sm^{3+}. For example, it is likely that the $^1G_4$ state, which is feeding the $^1D_2$ state, depopulates faster due to ET between Sm^{3+} and Tm^{3+}, thereby decreasing the UC efficiency, since the energy of the $^4I_{11/2}$ level of Sm^{3+} matches quite well with the $^1G_4$ level of Tm^{3+}. However, the absence of any characteristic Sm^{3+} emissions implies that the possibility of the ET is minute. From the energy diagram of the Sm^{3+} and Tm^{3+}, the cross-relaxation between the higher energy Tm^{3+} levels and lower energy Sm^{3+} levels likely play role in the greater reduction in the intensity of the 451 nm emission. One possibility might be the cross relaxation between $^1D_2$ (Tm^{3+})+$^6H_{3/2}$(Sm^{3+}) and $^1G_4$ (Tm^{3+})+$^6F_{3/2}$ (Sm^{3+}) that is schematically shown in Fig. 7(a). Unfortunately, the proposed cross relaxation process would lead to an increase in the population of the $^1G_4$ state of the Tm^{3+}, leading to the increase of the UC emission at 475 nm, which is inconsistent with our experiments. Hence, the decrease of the UC emission at 475 nm implies the possibility of additional non-radiative relaxation channels involving the low-lying energy levels of Tm^{3+} and Sm^{3+} ions, which reduces the UC efficiency. It is reasonable to consider the presence of an ET from $^3H_4$ (Tm^{3+}) to $^6F_{11/2}$ (Sm^{3+}) as these levels are closely matched in energy. Obviously, the ET from $^3H_4$ of Tm^{3+} to $^6F_{11/2}$ of Sm^{3+} also leads to a decrease in the intensity of the 800 nm emission. According to our experimental results, we consider that the influence of the ET from $^3H_4$ (Tm^{3+}) to $^6F_{11/2}$ (Sm^{3+}) on the UC process to populate $^1G_4$ state of the Tm^{3+} is more notable than that on the radiative transition to emit NIR emission of 800 nm at low Sm^{3+} doping concentration.

To further clarify the UC mechanisms, the power-dependent UC behaviors of the observed emissions are systematically investigated. Generally, the UC luminescence intensity (I_{UC}) is related to the pump infrared one (I_{IR}) via the formula, $I_{UP}\propto I_{IR}^n$, where n is the pump photon number required to populate the upper emitting level and its value can be obtained from the slope of the line in the plot of $\log(I_{UP})$ versus $\log(I_{IR})$ [13]. Fig. 7(b) shows the double-logarithmic plot of the UC emission intensity versus the pump power density of cubic Tm^{3+} (0.5 mol%) doped $KYb_{0.2}Gd_{0.8}F_4$ nanocrystals. The slope values of the linear fits with the experimental data are 2.64 and 1.74 for the observed blue emission at 475 nm and NIR emission at 800 nm, respectively. The results indicate that two and three pump photons are necessary to produce NIR emission at 800 nm and blue emission at 475 nm in cubic $KYb_{0.2}Gd_{0.8}F_4$ nanocrystals, which is consistent with our previous results [12]. Fig. 7(c) shows the double-logarithmic plot of the UC emission intensity versus the pump power density of Tm^{3+} (0.5 mol%) doped KYb_2F_7 nanocrystals. The slope values of the linear fits with the experimental data are 0.74 and 0.64 for the observed blue emission at 475 nm and NIR emission at 800 nm, respectively, under low pump power densities, implying the existence of strong saturation effect in Tm^{3+} (0.5 mol%) doped KYb_2F_7 nanocrystals. In KYb_2F_7 nanocrystals, the $^3H_4$ excited state of Tm^{3+} becomes saturated easily owing to the efficient ET processes from Yb^{3+} to Tm^{3+} due to the highest Yb^{3+} concentration in host, resulting in the following ET processes populating the upper $^1G_4$ excited

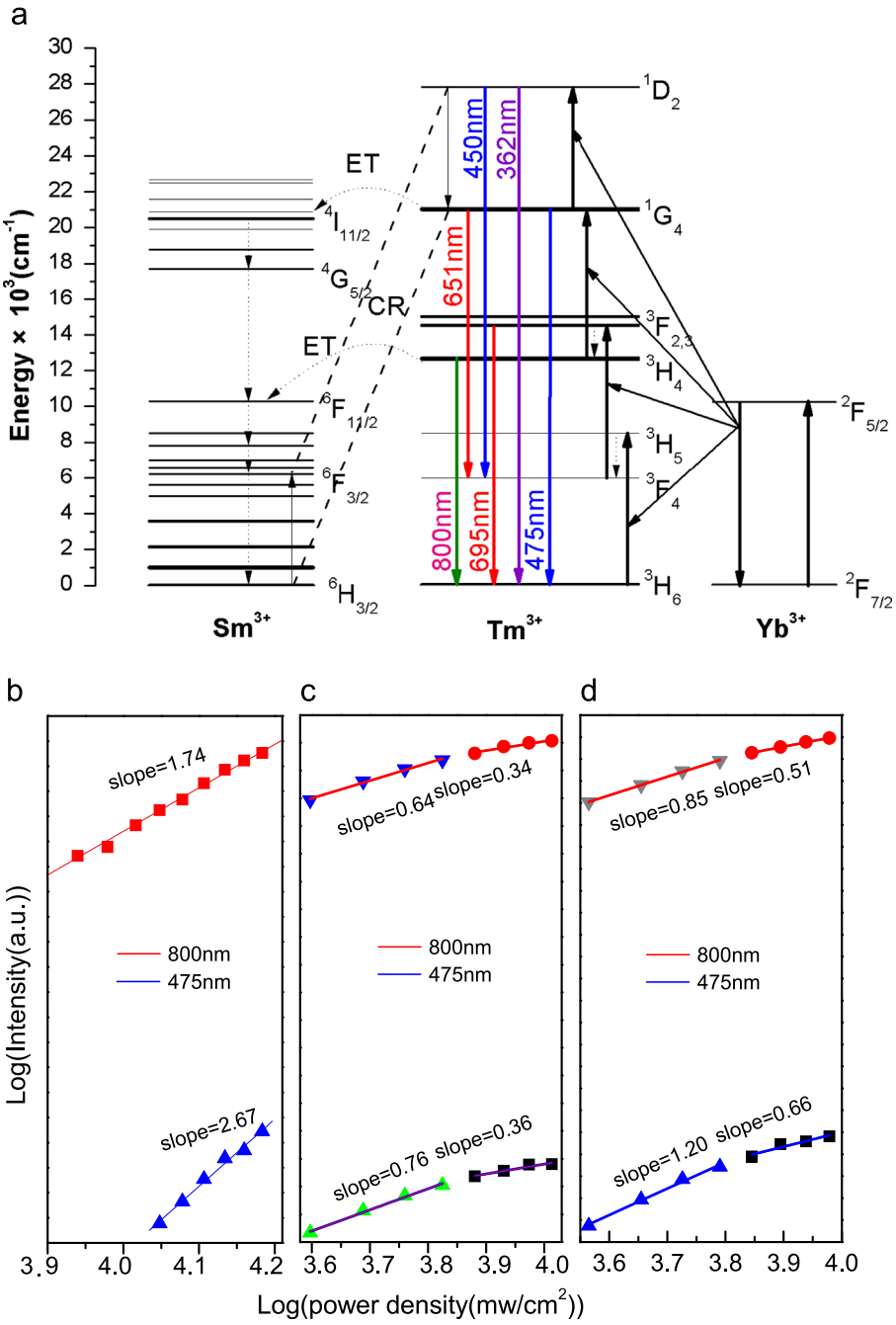

Fig. 7. (a) The energy diagram of the Yb^{3+}, Sm^{3+} and Tm^{3+} dopant ions and the possible UC mechanisms under the excitation of a 980 nm LD. (b)–(d) The double-logarithmic plots of the UC emission intensity versus the pump power density of cubic Tm^{3+} (0.5 mol%) doped $KYb_{0.2}Gd_{0.8}F_4$ nanocrystals, Tm^{3+} (0.5 mol%) doped KYb_2F_7 nanocrystals, and Tm^{3+} (0.5 mol%) doped KYb_2F_7 nanocrystals codoping with 0.05 mol% Sm^{3+}, respectively.

states being so efficient that it exceeds the spontaneous decay rate to the ground states. Furthermore, one can see that the slope values tend to decrease for the two observed UC emissions with increasing pump power densities. This saturation effect could be attributed to two factors [3,33,34]. One is the saturation of the Yb^{3+} absorption at high pump power densities. The other may be related to the further saturation of the $^3H_4$ excited states of Tm^{3+} at high pump power densities owing to the enhanced ET efficiency from Yb^{3+} to Tm^{3+}. Fig. 7(d) shows the double-logarithmic plot of the UC emission intensity versus the pump power density of Tm^{3+} (0.5 mol%) doped KYb_2F_7 nanocrystals co-doping with 0.05 mol% Sm^{3+}. Saturation-effect-induced decrease of slope values for blue and NIR emissions can be also observed at both low and high pump power densities. However, one can find that the slope values are rather high compared with those in Tm^{3+} (0.5 mol%) doped KYb_2F_7 nanocrystals. Usually,

the anomalous power dependence in UC materials has been fundamentally attributed to the competition between the UC rate and the linear decay due to the saturation effects of the low excited states [33]. Hence the results indicate that the saturation effects of the low excited states become depressed and the UC rate decrease due to the ET from $^3H_4$ (Tm^{3+}) to $^6F_{11/2}$ (Sm^{3+}) after the introduction of Sm^{3+} ions. Since the influence of Sm^{3+} doping on the UC process to populate higher $^1G_4$ and $^1D_2$ excited states of Tm^{3+} is more notable than that on the radiative transition to emit NIR emission, selective suppression of the intensity of the higher energy emissions over the NIR emission is realized and NIR to visible emission ratios is enhanced via doping small concentrations of Sm^{3+} ions.

4. Conclusions

Tm^{3+} doped KF–YbF_3 nanocrystals with different Gd^{3+} concentrations are synthesized by a hydrothermal method using oleic acid as a stabilizing agent at 190 °C. The results of XRD and TEM indicate the phase and size of the as prepared Tm^{3+} doped KF–YbF_3 nanocrystals are closely related to the Gd^{3+} doping content. Without Gd^{3+} impurity, the undoped nanocrystals crystallize in orthorhombic KYb_2F_7 with an average diameter of 42 nm. The complete phase transformation from orthorhombic KYb_2F_7 to cubic $KGdF_4$ is observed in the final products after the Gd^{3+} doping concentration is beyond about 30 mol%. Under the excitation of a 980 nm LD, strong NIR UC emission at 800 nm can be observed from the obtained Tm^{3+} doped nanocrystals. Particularly, the intensities of high energy UV and blue UC emissions in Tm^{3+} doped KYb_2F_7 nanocrystals are selectively reduced compared to the NIR emission at 800 nm by co-doping a small amount of Sm^{3+} ions into the host matrix. The selective suppression of the intensity of the higher energy emissions over the NIR emission is attributed to the depression of saturation effect in Tm^{3+} doped KYb_2F_7 nanocrystals due to the ET from $^3H_4$ (Tm^{3+}) to $^6F_{11/2}$ (Sm^{3+}). Our results indicate that Tm^{3+}/Sm^{3+} co-doped KF–YbF_3 nanocrystals with a selective suppression of higher energy UC emissions over the NIR UC emission have potential applications in fluorescent bio-labels since they can enhance the contrast of the imaging process [24].

Acknowledgments

This work was supported by the Grants from National Natural Science Foundation of China (Nos. 51272220, 11275163 and 11204262) and the Open Fund based on the innovation platform of Hunan colleges and universities (No. 11K060).

References

[1] F. Auzel, Upconversion and anti-stokes processes with f and d ions in solids, Chemical Reviews 104 (2004) 139–174.

[2] F. Wang, Y. Han, C. Lim, Y. Lu, J. Wang, J. Xu, H. Chen, C. Zhang, M. Hong, X. Liu, Simultaneous phase and size control of upconversion nanocrystals through lanthanide doping, Nature 463 (2010) 1061–1065.

[3] C. Jacinto, M. Vermelho, E. Gouveia, M. de Araujo, P. Udo, N. Astrath, M. Baesso, Pump-power-controlled luminescence switching in Yb^{3+}/Tm^{3+} co-doped water-free low silica calcium aluminosilicate glasses, Applied Physics Letter 91 (2007) 071102.

[4] X. Huang, S. Han, W. Huang, X. Liu, Enhancing solar cell efficiency: the search for luminescent materials as spectral converters, Chemical Society Reviews 42 (2013) 173–201.

[5] B. van der Ende, L. Aartsa, A. Meijerink, Lanthanide ions as spectral converters for solar cells, Physical Chemistry Chemical Physics 11 (2009) 11081–11095.

[6] F. Wang, D. Banerjee, Y. Liu, X. Chen, X. Liu, Upconversion nanoparticles in biological labeling, imaging, and therapy, Analyst 135 (2010) 1839–1854.

[7] F. Wang, X. Liu, Recent advances in the chemistry of lanthanide-doped upconversion nano-crystals, Chemical Society Reviews 38 (2009) 976–989.

[8] J. Zhou, Z. Liu, F. Li, Upconversion nanophosphors for small-animal imaging, Chemical Society Reviews 41 (2012) 1323–1349.

[9] M. Haase, H. Schäfer, Upconverting nanoparticles, Angewandte Chemie International Edition 50 (2011) 5808–5829.

[10] C. Li, J. Lin, Rare earth fluoride nano-/micro-crystals: synthesis, surface modification and application, Journal of Materials Chemistry 20 (2010) 6831–6847.

[11] G. Wang, Q. Peng, Y. Li, Luminescence tuning of upconversion nanocrystals, Chemistry A European Journal 16 (2010) 4923–4931.

[12] L. Yang, Y. Zhang, J. Li, Y. Li, J. Zhong, P.K. Chu, Magnetic and upconverted luminescent properties of multifunctional lanthanide doped cubic $KGdF_4$ nanocrystals, Nanoscale 2 (2010) 2805–2810.

[13] L.W. Yang, H.L. Han, Y.Y. Zhang, J.X. Zhong, White emission by frequency up-conversion in Yb^{3+}–Ho^{3+}–Tm^{3+} triply doped hexagonal $NaYF_4n$ nanorods, Journal of Physical Chemistry C113 (2009) 18995–18999.

[14] L.W. Yang, Y. Li, Y.C. Li, J.J. Li, J.H. Hao, J.X. Zhong, P.K. Chu, Quasi-seeded growth, phase transformation, and size tuning of multifunctional hexagonal $NaLnF_4$ (Ln=Y, Gd, Yb) nanocrystals via in situ cation-exchange reaction, Journal of Materials Chemistry 22 (2012) 2254–2262.

[15] L.W. Yang, Y.C. Li, S.X. Yu, J.H. Hao, J.X. Zhong, P.K. Chu, Phase transformation and size tuning in controlled-growth of nanocrystals *via* self-seeded nucleation with preferential thermodynamic stability, Chemical Communications 47 (2011) 12544–12546.

[16] D. Chen, Y. Yu, F. Huang, A. Yang, Y. Wang, Lanthanide activator doped $NaYb_{1-x}Gd_xF_4$ nanocrystals with tunable down-, up-conversion luminescence and paramagnetic properties, Journal of Materials Chemistry 21 (2011) 6186–6192.

[17] G. Chen, H. Liu, G. Somesfalean, H. Liang, Z. Zhang, Upconversion emission tuning from green to red in Yb^{3+}/Ho^{3+}-codoped $NaYF_4$ nanocrystals by tridoping with Ce^{3+} ions, Nanotechnology 20 (2009) 385704.

[18] J. Boyer, L. Cuccia, J. Capobianco, Synthesis of colloidal upconverting $NaYF_4$:Er^{3+}/Yb^{3+} and Tm^{3+}/Yb^{3+} monodisperse nanocrystals, Nano Letters 7 (2007) 847–852.

[19] V. Mahalingam, F. Vetrone, R. Naccache, A. Speghini, J. Capobianco, Colloidal Tm^{3+}/Yb^{3+}-doped $LiYF_4$ nanocrystals: multiple luminescence spanning the UV to NIR regions via low energy excitation, Advances Materials 21 (2009) 4025–4028.

[20] D. Chen, Y. Yu, F. Huang, P. Huang, A. Yang, Y. Wang, Modifying the size and shape of monodisperse bifunctional alkaline-earth fluoride nanocrystals through lanthanide doping, Journal of the American Chemical Society 132 (2010) 9976–9978.

[21] D. Chen, Y. Yu, F. Huang, Y. Wang, Phase transition from hexagonal LnF_3 (Ln=La, Ce, Pr) to cubic $Ln_{0.8}M_{0.2}F_{2.8}$ (M=Ca, Sr, Ba)

nanocrystals with enhanced upconversion induced by alkaline-earth doping, Chemical Communications 47 (2011) 2601–2603.
[22] Q. Liu, Y. Sun, T. Yang, W. Feng, C. Li, F. Li, Sub-10 nm hexagonal lanthanide-doped $NaLuF_4$ upconversion nanocrystals for sensitive bioimaging in vivo, Journal of the American Chemical Society 133 (2011) 17122–17125.
[23] M. Nyk, R. Kumar, T. Ohulchanskyy, E. Bergey, P. Prasad, High contrast in Vitro and in Vivo photoluminescence bioimaging using near infrared to near infrared up-conversion in Tm^{3+} and Yb^{3+} doped fluoride nanophosphors, Nano Letters 8 (2008) 3834–3838.
[24] V. Mahalingam, R. Naccache, F. Vetrone, J.A. Capobianco, Preferential suppression of high-energy upconverted emissions of Tm^{3+} by Dy^{3+} ions in $Tm^{3+}/Dy^{3+}/Yb^{3+}$-doped $LiYF_4$ colloidal nanocrystals, Chemical Communications 47/12 (2011) 3481–3483.
[25] G.Y. Chen, T.Y. Ohulchanskyy, W.C. Law, H. Agren, P.N. Prasad, Monodisperse $NaYbF_4:Tm^{3+}/NaGdF_4$ core/shell nanocrystals with near-infrared to near-infrared upconversion photoluminescence and magnetic resonance properties, Nanoscale 3 (2011) 2003–2008.
[26] G. Chen, J. Shen, T.Y. Ohulchanskyy, N.J. Patel, A. Kutikov, Z. Li, J. Song, R.K. Pandey, H. Agren, P.N. Prasad, (α-$NaYbF_4:Tm^{3+}$)/CaF_2 core/shell nanoparticles with efficient near-infrared to near-infrared upconversion for high-contrast deep tissue bioimaging, ACS nano 6 (2012) 8280–8287.
[27] F. Wang, J. Wang, X. Liu, Direct evidence of a surface quenching effect on size-dependent luminescence of upconversion nanoparticles, Angewandte Chemie International Edition 49 (2010) 7456–7460.
[28] M. Banski, M. Afzaal, A. Podhorodecki, J. Misiewicz, A.L. Abdelhady, P. O'Brien, Passivation of lanthanide surface sites in sub-10 nm $NaYF4:Eu^{3+}$ nanocrystals, Journal of Nanoparticle Research 14 (2012) 1228.
[29] Q. Su, S. Han, X. Xie, H. Zhu, H. Chen, C. Chen, R.S. Liu, X.Y. Chen, F. Wang, X. Liu, The effect of surface coating on energy migration-mediated upconversion, Journal of the American Chemical Society 134 (2012) 20849–20857.
[30] J. Zhao, Z. Lu, Y. Yin, C. McRae, J.A. Pipe, J.M. Dawes, D. Jin, E.M. Goldys, Upconversion luminescence with tunable lifetime in $NaYF_4$:Yb,Er nanocrystals: role of nanocrystal size, Nanoscale 5 (2013) 944–952.
[31] J. Suyver, J. Grimm, M. Van Veen, D. Biner, K. Kramer, H. Gudel, Upconversion spectroscopy and properties of $NaYF_4$ doped with Er^{3+}, Tm^{3+} and/or Yb^3, Journal of Luminescence 117 (2006) 1–12.
[32] F. Vetrone, V. Mahalingam, J. Capobianco, Near-infrared-to-blue Uupconversion in colloidal BaYF5:Tm3+, Yb3+ nanocrystals, Chemistry of Materials 21 (2009) 1847–1851.
[33] M. Pollnau, D. Gamelin, S. Luthi, H. Gudel, M. Hehlen, Power dependence of upconversion luminescence in lanthanide and transition-metal-ion systems, Physical Review B 61 (2000) 3337–3346.
[34] J. Li, L. Yang, Y. Zhang, J. Zhong, C.Q. Sun, P.K. Chu, Pump-power tunable white upconversion emission in lanthanide-doped hexagonal $NaFY_4$ nanorods, Optical Materials 33 (2011) 882–887.